Chinese Chemical Letters 35 (2024) 109122

Contents lists available at ScienceDirect

Chinese Chemical Letters

journal homepage: www.elsevier.com/locate/cclet

# An intermittent lithium deposition model based on bimetallic MOFs derivatives for dendrite-free lithium anode with ultrahigh areal capacity

Tao Wei[a,1,*], Jiahao Lu[a,d,1], Pan Zhang[b,1], Qi Zhang[a,e,1], Guang Yang[b], Ruizhi Yang[d], Daifen Chen[a], Qian Wang[c,*], Yongfu Tang[b,*]

[a] School of Energy and Power, Jiangsu University of Science and Technology, Zhenjiang 212003, China
[b] State Key Laboratory of Metastable Materials Science and Technology (MMST), Hebei Key Laboratory of Applied Chemistry, Yanshan University, Qinhuangdao 066004, China
[c] College of Materials Science and Engineering, Taiyuan University of Technology, Taiyuan 030024, China
[d] College of Energy, Soochow University, Suzhou 215006, China
[e] School of Low-carbon Energy and Power Engineering, China University of Mining and Technology, Xuzhou 221116, China

ARTICLE INFO

*Article history:*
Received 31 July 2023
Revised 23 August 2023
Accepted 18 September 2023
Available online 22 September 2023

*Keywords:*
Intermittent lithiophilic model
Lithium metal anode (LMA)
Three-dimensional (3D) frameworks
Lithiophilic
Bimetallic metal-organic frameworks (MOFs)

ABSTRACT

In the development of 3D conductive frameworks for lithium metal anode (LMA), two models have been proposed: top growth model and bottom-up growth model. However, Li tends to accumulate on the top of these 3D frameworks with homogenous lithiophilicity (top growth) and Li dendrite still forms. To address this issue, some researchers have focused on developing 3D frameworks with gradient lithiophilicity, which realized bottom-up growth of Li. Nevertheless, partial Li nucleation sites on the top of these frameworks were missed. Inspired by the two models talked above, this work firstly proposed a novel intermittent lithiophilic model for lithium deposition. To demonstrate the feasibility of this model, a bimetallic metal-organic frameworks derived $ZnMn_2O_4$-MnO nanoparticles were grown on carbon cloth for LMA. It can cycle stably under ultra-high current and areal capacity (10 mA/cm$^2$, 10 mAh/cm$^2$). The *in-situ* optical microscopy (OM) was conducted to observe the Li deposition behavior, no dendrite was found during 80 h in ester-based electrolyte while the pure Li only cycled for 2 h. What is more, it can also be well-coupled with $LiNi_{0.8}Co_{0.1}Mn_{0.1}O_2$ (NCM811) cathode and solid-state electrolyte, which further prove the advantages of the intermittent model for the development of LMAs with high safety and high energy density.

Since Sony Co. made lithium (Li)-ion batteries (LIBs) available to the public in 1991, it has exerted great influence on modern society [1–5]. Nevertheless, the energy density of graphite-based anode is getting close to its limit, thus new electrode materials and battery systems need to be developed [6–9]. For a long time, the Li metal anode (LMA) has been considered as the “holy grail” in Li secondary batteries owing to the ultrahigh theoretical capacity (3860 mAh/g) and the lowest electrochemical potential (−3.04 V *vs.* $H^+/H_2$), which provides a prospective solution for new-generation rechargeable batteries [10–15]. Unfortunately, the practical applications of LMAs still remain grand challenges due to the continuous growth of Li dendrites and unlimited volume change [16,17].

In 2016, Cui *et al.* [18–20] have put the pioneering works by constructing a novel composite anode for LMA by allowing molten Li seep into lithiophilic 3D frameworks. From then on, 3D conductive frameworks (Ni foam (NF) [21–24], Cu foam (CF) [25–28] and 3D carbon-based hosts [29–32]) have been developed and show their enormous potential to restrain the dendritic growth and volume expansion owing to their high conductivities and porous structures. For example, our previous work uniformly coated a ZIF-67 derived $Co_3O_4$ layer on NF frameworks by one pot method, and then infused molten Li into $Co_3O_4$-NF framework to obtain Li-$Co_3O_4$-NF composite anode [33]. It showed a relative uniform Li deposition behavior in ether-based electrolyte (stabilized at 3 mA/cm$^2$, 1.5 mAh/cm$^2$), but there were still some Li dendrites could be observed through the *in-situ* OM. According to previous

---

[*] Corresponding authors.
*E-mail addresses:* wt863@just.edu.cn (T. Wei), qianwang0825@pku.edu.cn (Q. Wang), tangyongfu@ysu.edu.cn (Y. Tang).
[1] These authors contribute equally to this work.

https://doi.org/10.1016/j.cclet.2023.109122

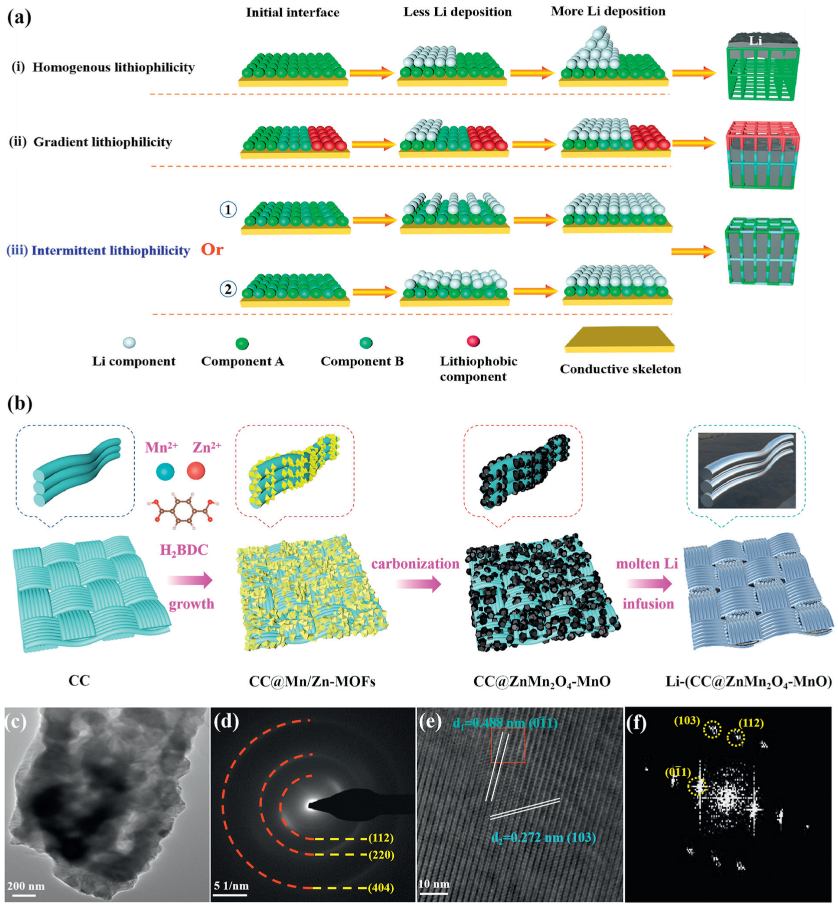

**Fig. 1.** (a) Mechanism diagram of Li component deposition on conductive frameworks with different interfacial activities: (i) homogenous interfaces (top growth); (ii) gradient interfaces (bottom-up growth); (iii) intermittent interfaces. (b) Schematic illustration of the preparation processes of the Li-(CC@$ZnMn_2O_4$-MnO) composite anode. Characterizations of the CC@$ZnMn_2O_4$-MnO electrodes. (c) TEM image; (d) SAED pattern; (e, f) HRTEM images. The tested particles were scraped off from CC@$ZnMn_2O_4$-MnO electrodes.

studies [34–35], this might be attributed to the fact that Li tends to accumulate on the top of these 3D frameworks with homogenous lithiophilicity (Fig. 1a(i)).

To address this issue of the accumulation of Li, more and more researchers have focused on developing 3D frameworks with gradient lithiophilicity [36–43], *i.e.*, the top region of the framework is lithiophobic or the lithiophilicity is reduced, thus suppressing the $Li^+$ reduction reaction on the top. By contrast, the bottom is lithiophilic, which realized bottom-up growth of Li. Nevertheless, for the reason of the top region is lithiophobic, partial Li nucleation sites on the top of these frameworks were missed (Fig. 1a(ii)). Thus, most of the gradient frameworks cannot exhibit higher capacities (Table S1 in Supporting information).

Inspired by the previous works talked above, this work firstly proposed a novel model for Li deposition, which was denoted as an intermittent lithiophilic model (Fig. 1a(iii)). It is constructed by two lithiophilic materials (A and B) intermittently arranged on the 3D conductive skeletons in the micro or nano scale. In this model, the lithiophilicity of A is better than that of B, thus the nucleation barrier of Li on A is smaller than that on B, so that $Li^+$ preferentially nucleates on component A and start to grow. Meanwhile, the concentration of $Li^+$ in electrolyte around A decreases, and the remaining $Li^+$ starts to nucleate and grow on component B under the synergist effect of lithiophilicity of B and higher concentration of $Li^+$. This way can not only effectively avoid Li accumulation in local areas of the skeletons, but also make full use of the entire 3D conductive frameworks as the nucleation sites of Li. A flat and compact Li layer was formed by the intergranular fusion between the Li embryos deposited in the early stage, which further promoted the stable deposition of the subsequent Li instead of the formation of dendrites [44].

To demonstrate the feasibility of this model, a bimetallic metal-organic frameworks (MOFs) (Mn/Zn-MOFs) derived $ZnMn_2O_4$-MnO nanoparticles were grown on carbon cloth (CC) substrates (CC@$ZnMn_2O_4$-MnO) as a 3D host for LMA. As MOFs are a kind of nano materials with unique intermittent arrangement because their adjacent metal atoms are separated by ligands (Fig. S1a in Supporting information) [45–48]. Compared with monometallic MOFs, bimetallic MOFs offer enhanced electrochemical performance, which can be ascribed to the synergistic effect between different metals and the adjustable metal node engineering. Metal substitution on the metal nodes in bimetallic MOFs can have advantages in tuning the stability, flexibility, and electronic structures of the material [49]. Moreover, carbonized MOFs derivatives can also inherit the main structure of MOFs [50,51]. These characteristics facilitate for a 200-h lifespan in the symmetrical cell with an ultrahigh areal capacity (10 $mAh/cm^2$) and current density (10 $mA/cm^2$) and a steady cycle performance at 20 C for 1000 cycles in ester-based electrolyte. Moreover, it can also be matched well with $LiNi_{0.8}Co_{0.1}Mn_{0.1}O_2$ (NCM811) cathode and solid electrolyte, which further prove the advantages of the intermittent model for the development of LMA with safety and high energy density.

Fig. 1b vividly describes the preparation processes of Li-(CC@$ZnMn_2O_4$-MnO) composite anode by a thermal infusing method. Briefly, Mn/Zn-MOFs were *in-situ* grown onto the CC *via* a facile solvothermal method by mixing a given amount of $Mn^{2+}/Zn^{2+}$ and terephthalic acid ($H_2BDC$) to obtain CC@Mn/Zn-MOFs, which is possible for scalable production. After heat treatment in $N_2$ atmosphere, the nano Mn/Zn-MOFs were transformed into $ZnMn_2O_4$-MnO (Fig. S1 in Supporting information). Experimental details can be seen in Supporting information. The lithiophilicity of CC can be efficiently improved by these coated nanosized lithiophilic $ZnMn_2O_4$-MnO materials, allowing molten Li to be introduced into the frameworks rapidly in only 7 s (Fig. S2 in Supporting information) [52]. For comparison, the molten Li cannot infiltrate into pure CC even after 60 s at the same temperature.

To analyze the crystal structure of the Mn/Zn-MOFs and their derivatives, they were both characterized *via* powder X-ray diffraction (XRD). The appeared main peaks of Mn/Zn-MOFs (Fig. S1b) is consistent with the simulated results. After the carbonization process (Fig. S1c), all the major diffraction peaks can be well-indexed with the $ZnMn_2O_4$ (PDF#24-1133) and MnO (PDF#07-0230), indicating the co-existence of $ZnMn_2O_4$ and MnO by the direct pyrolysis of the Mn/Zn-MOFs.

Fig. 1c shows the TEM images of the $ZnMn_2O_4$-MnO after the carbonization of Mn/Zn-MOFs. The SAED patterns of $ZnMn_2O_4$ particles displayed the (112), (220), (404) planes (Fig. 1d), which demonstrated the presence of $ZnMn_2O_4$. As can be clearly observed in the HRTEM images (Figs. 1e and f), two clear lattice fringes about 0.272 nm, 0.488 nm are corresponded to the (103), $(0\bar{1}1)$ planes of $ZnMn_2O_4$ with $[\bar{3}11]$ zone axis. Additionally, to confirm the chemical components of the CC@$ZnMn_2O_4$-MnO host, X-ray photoelectron spectroscopy (XPS) was conducted and the corresponding results are depicted in Fig. S3 (Supporting information). It could be clearly demonstrated that the existence of C, Zn, O, and Mn elements. The C 1s spectra is shown in Fig. S3a, with two distinct peaks at 284.8 eV (representing the normal C–C $sp^2$-hybridization bonding in graphitic carbon) and 287.9 eV (attributed to the functionalized O=C–O bond). Furthermore, two peaks at 1022.6 eV (Zn $2p_{3/2}$) and 1045.7 eV (Zn $2p_{1/2}$) can be identified to the existence of $Zn^{2+}$ in the host (Fig. S3b). In the meantime, three significant peaks at 531.0 eV, 531.5 eV, and 531.8 eV in the high-resolution O 1s peak (Fig. S3c), which correspond to the Mn-O, Zn-O, and C–O bonds, respectively. Most importantly, the peaks at 641.7 eV and 653.0 eV reveal the existence of the $Mn^{3+}$, and the peaks at 643.5 eV and 654.8 eV are relevant to the $Mn^{2+}$ in the product (Fig. S3d). These results indicate the formation of $ZnMn_2O_4$ and MnO after carbonization which in well agreement with the XRD results.

The morphologies of the as-prepared CC, CC@Mn/Zn-MOFs, CC@$ZnMn_2O_4$-MnO, Li-(CC@$ZnMn_2O_4$-MnO) were determined by digital photos and SEM (Fig. 2). Fig. 2a shows the digital photos of different steps. It is clearly that the color of CC host changed from white (CC@Mn/Zn-MOFs) to brown (CC@$ZnMn_2O_4$-MnO) after the carbonization process under high temperature. From the SEM results, the pure CC host has a smooth surface (Figs. 2b and c), after the hydrothermal process, Mn/Zn-MOFs were tightly and uniformly coated on the CC fibers (Figs. 2d and e). Then after the heating treatment, the Mn/Zn-MOFs were transformed to $ZnMn_2O_4$-MnO and the CC structure was well maintained. The diameters of the bimetallic MOFs-derived nanoparticles are approximately 600–700 nm (Figs. 2f and g). After infusion of Li, it can be clearly seen that Li was fully immersed into the 3D CC host observing from the surface and cross-sectional view (Figs. 2h–k), which indicates that the coated $ZnMn_2O_4$-MnO particles effectively improve the Li affinity of CC host. Moreover, it can be proved from the EDS elemental mapping images that the Mn, Zn, O elements were uniformly distributed on the surface of CC (Fig. 2l).

For the purpose of investigating the electrochemical reversibility of the 3D CC@$ZnMn_2O_4$-MnO host, two different half cells (CC@$ZnMn_2O_4$-MnO and pure CC) were assembled and utilized to explore the cyclic stability of the Coulombic efficiency (CE) (Figs. 3a–c). The CC@$ZnMn_2O_4$-MnO composite host showed a higher CE of 99.45 % than the pure CC host and could guarantee ~560 cycles at 1 $mA/cm^2$, 1 $mAh/cm^2$ (Fig. 3a). Moreover, when the current density increased to 3 $mA/cm^2$ and 5 $mA/cm^2$ (Figs. 3b and c), the CC@$ZnMn_2O_4$-MnO composite host still retain a high CE close to 98% for ~360 and ~200 cycles, respectively. The superior stability of CC@$ZnMn_2O_4$-MnO composite host than that of pure CC host should be ascribed to the full utilization of Li nucleation sites of 3D CC substrates through lithiophilic $ZnMn_2O_4$-MnO nanoparticles.

To further evaluating the Li deposition behavior on the CC@$ZnMn_2O_4$-MnO host during the repetitive charging/discharging processes, two kinds of symmetric cells (Li||Li, Li-(CC@$ZnMn_2O_4$-MnO)||Li-(CC@$ZnMn_2O_4$-MnO)) were then assembled with ether liquid electrolyte (Figs. 3d–g). Fig. 3d depicted the voltage-time curves of these two different cells at 3 $mA/cm^2$, 1 $mAh/cm^2$. Remarkably, the Li-(CC@$ZnMn_2O_4$-MnO) symmetric cell presented a stable voltage plateau with a small overpotential of ~20 mV. Meanwhile, it could maintain more than 1000 h. For comparison, the pure Li foil counterpart exhibited a fluctuant voltage curve with much larger overpotential. In addition, these two symmetric cells were also conducted at 3 $mA/cm^2$, 3 $mAh/cm^2$ (Fig. 3e). Obviously, the Li-(CC@$ZnMn_2O_4$-MnO) symmetric cells still depicted flat charge-discharge profiles with a smaller overpotential (stable cycle for over 600 h) than pure Li foil symmetric cells (short-circuited after 300 h) and the details were magnified to display the differences of the voltage hysteresis. When they were cycled at 10 $mA/cm^2$, 10 $mAh/cm^2$ (Fig. 3f), the Li-(CC@$ZnMn_2O_4$-MnO) symmetric cells could still show a relatively low overpotential of ~150 mV for about 200 h. By contrast, the pure Li||Li symmetric cell was directly short-circuited under such a high current density. To verify the superior electrochemical reversibility of Li-(CC@$ZnMn_2O_4$-MnO) electrodes, the rate performances were tested. The Li-(CC@$ZnMn_2O_4$-MnO) symmetric cells revealed a voltage polarization of 15, 90, and 144 mV at a current density of 0.5, 5, 12 $mA/cm^2$, respectively (Fig. 3g). Nevertheless, the pure Li||Li symmetric cell (Fig. S4 in Supporting information) could only cycle at 5 $mA/cm^2$ and the voltage polarization was unstable, which might be attributed to the continuous growth of Li dendrite [53–56]. From here we can clearly see that the improved electrochemical performances of the Li-(CC@$ZnMn_2O_4$-MnO) electrode, which was benefited from the synergist effect of lithiophilic $ZnMn_2O_4$ and MnO on the intermittent lithiophilic model.

Electrochemical impedance spectroscopy (EIS) for both pure Li and Li-(CC@$ZnMn_2O_4$-MnO) symmetric cells (Fig. S5 and Table S2 in Supporting information) were performed before and after cycling. It is apparent that the pure Li symmetric cell has a large interfacial resistance (208 Ω), which was due to the passivation layer on the surface of Li foil [57]. In comparison, the smaller interfacial resistances were obtained for the Li-(CC@$ZnMn_2O_4$-MnO) symmetric cell, which was 44.9 Ω at initial and 16.1 Ω after 100 cycles. This phenomenon was originated from the regulated Li deposition brought by Li-(CC@$ZnMn_2O_4$-MnO) electrodes. These findings also support the capability of the Li-(CC@$ZnMn_2O_4$-MnO) electrode in regulating the Li deposition behavior.

To evaluate the practical applications of Li-(CC@$ZnMn_2O_4$-MnO) electrodes, it was matched with $LiFePO_4$ (LFP) cathode to obtain a full cell (Li-(CC@$ZnMn_2O_4$-MnO)||LFP). Furthermore, two full cells with LFP cathode (Li-CC@MnO||LFP, Li-CC@$ZnMn_2O_4$||LFP) were also assembled and cycled at 5 C (Fig. S6 in Supporting information) for comparation. Comparing the results of Fig. S6 with that of Fig. 3h, the Li-(CC@$ZnMn_2O_4$-MnO)||LFP full cell has a more remarkable cycling stability. In addition, no matter at any current density (between 2 C and 20 C), the Li-(CC@$ZnMn_2O_4$-MnO)||LFP full cell can maintain about 1000 cycles nearly without capacity loss. Simultaneously, the Li-(CC@$ZnMn_2O_4$-MnO)||LFP full cell has a

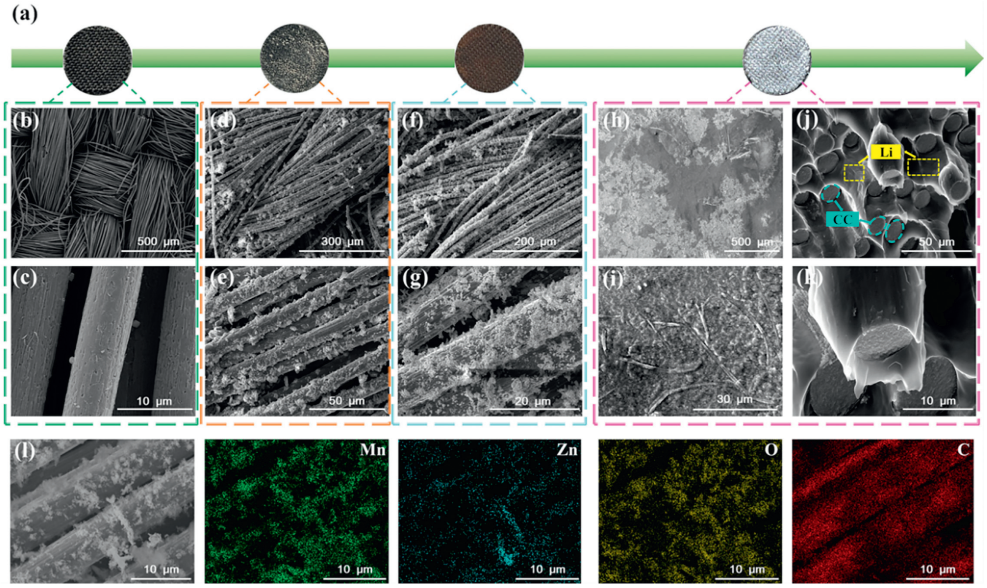

**Fig. 2.** The morphologies characterizations. (a) Digital photos of the different steps. SEM images of (b, c) CC, (d, e) CC@Mn/Zn-MOFs, (f, g) CC@$ZnMn_2O_4$-MnO, Li-(CC@$ZnMn_2O_4$-MnO) ((h, i) Surface; (j, k) cross-section). (l) EDS elements distribution of the CC@$ZnMn_2O_4$-MnO electrode (Mn, Zn, O, C).

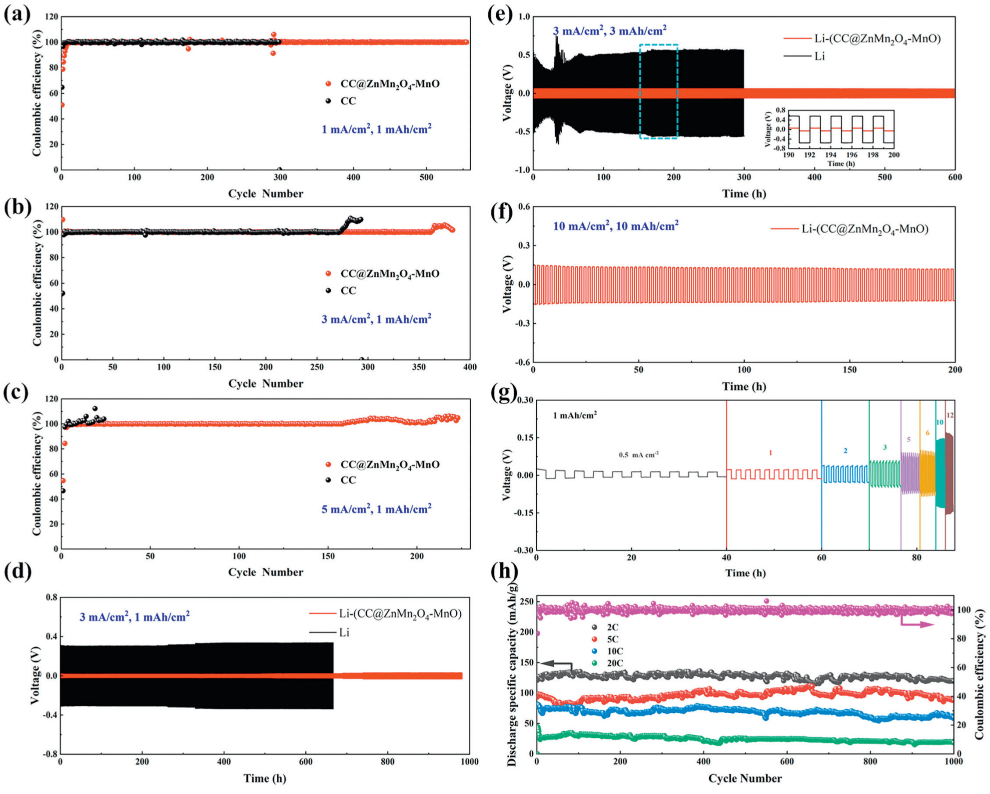

**Fig. 3.** Coulombic efficiency at various current densities of the CC and CC@$ZnMn_2O_4$-MnO electrode with 1 mAh/$cm^2$. (a) 1 mA/$cm^2$, (b) 3 mA/$cm^2$, (c) 5 mA/$cm^2$. Electrochemical performance comparisons of the Li-(CC@$ZnMn_2O_4$-MnO) (red) and pure Li foil (black) symmetric cells. Cyclic stabilities with different Li capacities at various current densities of (d) 3 mA/$cm^2$, 1 mAh/$cm^2$, (e) 3 mA/$cm^2$, 3 mAh/$cm^2$, (f) 10 mA/$cm^2$, 10 mAh/$cm^2$. (g) Rate performance of symmetric Li cells with Li-(CC@$ZnMn_2O_4$-MnO) electrodes (1 mAh/$cm^2$) at various current densities. (h) Long-term cycling performances of Li-(CC@$ZnMn_2O_4$-MnO)||LFP full cells from 2 C to 20 C (1 C = 170 mAh/g).

relative low potential for polarization during both charge and discharge processes (Fig. S7 in Supporting information). Capacities of ~100 mAh/g and ~70 mAh/g were preserved even at a high current rate of 5 C and 10 C (Fig. 3h). Additionally, the CE of the Li-(CC@$ZnMn_2O_4$-MnO) electrode maintained a steady value around 100% during cycling, which further prove the feasibility of the Li-(CC@$ZnMn_2O_4$-MnO) as the intermittent Li deposition model and achieve superior electrochemical performances.

To further study the mechanism of suppressing the Li dendrite in the Li-(CC@$ZnMn_2O_4$-MnO) composite anode, the *in situ* optical microscope (OM) was conducted to observe the Li plating/stripping processes in ester-based electrolyte (Fig. 4) [58]. Fig. 4a shows the performance of pure Li. During the first charging process, the Li dendrite is formed at a fast speed in the local area of the exposed Li surface (Fig. 4a, I–VI). Moreover, the growth of these dendrites is relatively disordered, which means the Li deposition process is

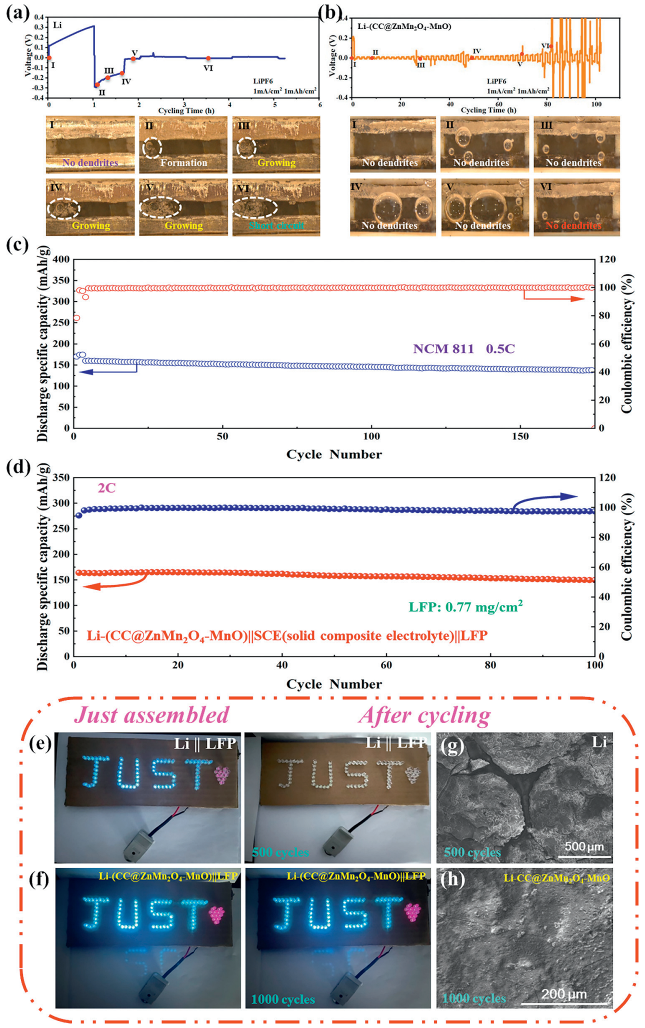

**Fig. 4.** *In situ* optical photographs of (a) pure Li and (b) Li-(CC@$ZnMn_2O_4$-MnO) electroplating process at different times at a current density of 1 mA/cm$^2$ in the Ester liquid electrolyte ($LiPF_6$: Ester-based electrolyte). Electrochemical performance of full cells. (c) Long-term cycling performance of Li-(CC@$ZnMn_2O_4$-MnO)||NCM811 full cells at 0.5 C (1 C = 180 mAh/g). (d) Long-term cycling performance of Li-(CC@$ZnMn_2O_4$-MnO) in all-solid-state lithium-ion batteries (Li-(CC@$ZnMn_2O_4$-MnO||SCE(solid composite electrolyte)||LFP) at 2 C. Illuminated LED lights powered by (e) Li||LFP and (f) Li-(CC@$ZnMn_2O_4$-MnO)||LFP full cells. SEM images after cycling in different full cells. (g) Li||LFP, (h) Li-(CC@$ZnMn_2O_4$-MnO)||LFP full cells.

uneven. Even worse, it only cycled for 2 h and soon became short-circuited, which not only results in the loss and the cracks of the SEI layer, but also gives rise to the degradation of the Li electrode. On the contrary, there were fewer changes and even no dendrite growth until 80 h on the Li-(CC@$ZnMn_2O_4$-MnO) composite anode (Fig. 4b), indicating that Li was uniformly deposited and the Li dendrite was effectively suppressed [59,60]. Thus, the presence of Li-(CC@$ZnMn_2O_4$-MnO) and its 3D structure evolution during the cycles played a crucial role in the Li plating/stripping behavior and the electrochemical performance of Li electrodes. What is more, the overpotential of Li-(CC@$ZnMn_2O_4$-MnO) was obviously decreased, and the polarization phenomenon appeared until cycling for over 80 h. Although *in situ* OM technology has its own limitations [58], but the results can be taken into account.

To further demonstrate the feasibility of the intermittent Li deposition model, similar running trend was observed in the Li-NCM811 batteries. The Li-(CC@$ZnMn_2O_4$-MnO)||NCM811 cell presented a stable discharge capacity of 137.4 mAh/g after more than 175 cycles at 0.5 C (Fig. 4c), which is significantly improved compared with cycling performance of the pure Li||NCM811 battery (Fig. S8 in Supporting information). Moreover, the Li-(CC@$ZnMn_2O_4$-MnO)||NCM811 cells also exhibit a superior rate performance. While cycling at different current densities of 0.1, 0.2, 0.5, 1 and 2 C, the Li-(CC@$ZnMn_2O_4$-MnO)||NCM811 cells can reach 178.1, 168.8, 149.7, 131.5 and 108.7 mAh/g, respectively (Fig. S9 in Supporting information). Additionally, compared with the previous reported MOF-derived modified CC hosts and gradient 3D frameworks (Fig. S10 in Supporting information), the Li-(CC@$ZnMn_2O_4$-MnO) composite anode gives the most available choice in practical application, which is benefited from a more stable cycling performance in ester-based electrolyte even in a higher current density and a larger areal capacity. What is more, the Li-(CC@$ZnMn_2O_4$-MnO) composite anode was applied in an all-solid-state Li battery (without liquid electrolyte) and showed an excellent cycling performance of ~160 mAh/g in 100 cycles at 2 C (Fig. 4d), which further implies that the possibility and feasibility of using the Li-(CC@$ZnMn_2O_4$-MnO) anodes in practical Li batteries in the future.

Besides, the practical applications of pure Li and Li-(CC@$ZnMn_2O_4$-MnO) anodes were also evaluated *via* lighting the light emitting diode (LED) by Li||LFP and Li-(CC@$ZnMn_2O_4$-MnO)||LFP coin cells. The evolution of LED brightness powered by different full cells are consistent with their electrochemical results (Figs. 4e and f). After cycling in full cells, the SEM images of the Li and Li-(CC@$ZnMn_2O_4$-MnO) electrodes were shown in Figs. 4g and h. Obviously, the surface of the Li-(CC@$ZnMn_2O_4$-MnO) composite anode is flat without any visible cracks, which indicates that a stable and uniform Li deposition behavior was performed during the long-term cycles and there were no Li dendrites growing. In contrast, the pure Li foil exhibited a worse performance, which is corresponded to the electrochemical results. These results further demonstrated the intermittent lithiophilic model obtained from bimetallic MOFs derivatives is an effective way to achieve the safer Li metal batteries.

To sum up, a novel intermittent lithiophilic model for Li deposition was firstly proposed. Based on this model, a bimetallic MOFs (Mn/Zn-MOFs) derived $ZnMn_2O_4$ and MnO were grown on CC substrates (CC@$ZnMn_2O_4$-MnO) as a 3D host for LMA. It can afford a prolonged lifespan of 200 h under an ultrahigh areal capacity (10 mAh/cm$^2$) and current density (10 mA/cm$^2$) and a stable cycle performance at 20 C for 1000 cycles in ester-based electrolyte. The Li-(CC@$ZnMn_2O_4$-MnO) symmetric cells exhibited a maximum current density of 12 mA/cm$^2$ at 1 mAh/cm$^2$. What is more, it can also be well-coupled with $LiNi_{0.8}Co_{0.1}Mn_{0.1}O_2$ cathode and solid-state electrolyte, which further prove the advantages of the intermittent model. We are firmly convinced that this work will provide us an innovative pathway for the development of high safety and high energy density LMAs, and give effective experimental and theoretical supports.

## Declaration of competing interest

The authors declare no competing financial interest.

## Acknowledgments

This work was financially supported by National Natural Science Foundation of China (Nos. 21701083, 22279112), Fok Ying-Tong Education Foundation of China (No. 171064), Natural Science Foundation of Hebei Province (Nos. B2022203018, B2018203297).

## Supplementary materials

Supplementary material associated with this article can be found, in the online version, at doi:10.1016/j.cclet.2023.109122.

## References

[1] M. Winter, B. Barnett, K. Xu, Chem. Rev. 118 (2018) 11433–11456.
[2] M. Li, J. Lu, Z. Chen, et al., Adv. Mater. 30 (2018) e1800561.
[3] P. Wang, Y. You, Y. Yin, et al., Adv. Energy Mater. 8 (2018) 1701912.
[4] T. Wei, Z. Zhang, Z. Wang, et al., ACS Appl. Energy Mater. 3 (2020) 9428–9435.
[5] T. Wei, Z. Zhang, Q. Zhang, et al., Int. J. Miner. Metall. Mater. 28 (2021) 1636–1646.
[6] Y. Sun, N. Liu, Y. Cui, Nat. Energy 1 (2016) 16071.
[7] B. Dunn, H. Kamath, J. Tarascon, Science 334 (2011) 928–935.
[8] Q. Cheng, Z. Chen, X. Li, et al., J. Energy Chem. 76 (2023) 181–186.
[9] Y. Song, L. Shen, N. Yao, et al., Chem 8 (2022) 3031–3050.
[10] P. Zou, Y. Sui, H. Zhan, et al., Chem. Rev. 121 (2021) 5986–6056.
[11] X. Chen, Y. Yao, C. Yan, et al., Angew. Chem. Int. Ed. 59 (2020) 7743–7747.
[12] T. Wei, J. Lu, M. Wang, et al., Chin. J. Chem. 41 (2023) 1861–1874.
[13] T. Wei, Y. Zhou, C. Sun, et al., Particuology 84 (2024) 89–97.
[14] Z. Chen, M. Zhao, L. Hou, et al., Adv. Mater. 34 (2022) 2201555.
[15] J. Liu, C. Zhao, D. Ren, et al., Adv. Mater. 34 (2022) 2109407.
[16] T. Wei, Y. Zhou, C. Sun, et al., Nano Res. 17 (2024) 2763–2769.
[17] J. Lang, Y. Long, J. Qu, et al., Energy Storage Mater. 16 (2019) 85–90.
[18] Y. Liu, D. Lin, Z. Liang, et al., Nat. Commun. 7 (2016) 10992.
[19] D. Lin, Y. Liu, Z. Liang, et al., Nat. Nanotechnol. 11 (2016) 626–632.
[20] Z. Liang, D. Lin, J. Zhao, et al., Proc. Natl. Acad. Sci. U. S. A. 113 (2016) 2862–2867.
[21] Q. Zhang, W. Bai, C. Sun, et al., Chem. Eng. J. 405 (2021) 127022.
[22] G. Huang, P. Guo, J. Wang, et al., Chem. Eng. J. 384 (2020) 123313.
[23] Y. Fan, X. He, H. Li, et al., Chem. Eng. J. 450 (2022) 138384.
[24] F. Zhao, X. Zhou, W. Deng, et al., Nano Energy 62 (2019) 55–63.
[25] W. Zhu, W. Deng, F. Zhao, et al., Energy Storage Mater. 21 (2019) 107–114.
[26] L. Qin, H. Xu, D. Wang, et al., ACS Appl. Mater. Interfaces 10 (2018) 27764–27770.
[27] L. Dong, Y. Zhang, Y. Lu, et al., Chem. Commun. 57 (2021) 8937–8940.
[28] Y. Cai, B. Qin, J. Lin, et al., ACS Appl. Mater. Interfaces 13 (2021) 23803–23810.
[29] S. Zhang, S. Xiao, D. Li, et al., Energy Storage Mater. 48 (2022) 172–190.
[30] X. Yan, L. Lin, Q. Chen, et al., Carbon Energy 3 (2021) 303–329.
[31] J. Sun, Y. Cheng, H. Zhang, et al., Nano Lett. 22 (2022) 5874–5882.
[32] S. Chen, S. Chen, D. Han, et al., Chemistry 28 (2022) e202201580.
[33] T. Wei, J. Lu, P. Zhang, et al., Chin. Chem. Lett. 34 (2022) 107947.
[34] H. Zhang, X. Liao, Y. Guan, et al., Nat. Commun. 9 (2018) 3729.
[35] J. Yun, B. Park, E. Won, et al., ACS Energy Lett. 5 (2020) 3108–3114.
[36] J. Zhou, F. Wu, G. Wei, et al., J. Power Sources 495 (2021) 229773.
[37] Y. Zhao, L. Wang, J. Zou, et al., J. Energy Chem. 65 (2022) 666–673.
[38] C. Zhang, R. Lyu, Wei. Lv, et al., Adv. Mater. 31 (2019) e1904991.
[39] X. Yan, Q. Zhang, W. Xu, et al., J. Mater. Chem. A 8 (2020) 1678–1686.
[40] J. Pu, J. Li, K. Zhang, et al., Nat. Commun. 10 (2019) 1896.
[41] Y. Nan, S. Li, Y. Shi, et al., Small 15 (2019) e1903520.
[42] Y. Lv, Q. Zhang, C. Li, et al., ACS Sustain. Chem. Eng. 10 (2022) 7188–7195.
[43] X. Cheng, J. Ban, Q. Wang, et al., Appl. Surf. Sci. 563 (2021) 150247.
[44] L. Qin, Y. Wu, M. Shen, et al., Energy Storage Mater. 44 (2022) 278–284.
[45] T. Wei, Q. Zhang, S. Wang, et al., Int. J. Miner. Metall. Mater. 30 (2023) 1897–1905.
[46] Q. Zhang, S. Wang, Y. Liu, et al., Energy Technol. 11 (2023) 2201438.
[47] J. Lu, Z. Wang, Q. Zhang, et al., Chin. J. Chem. Eng. 60 (2023) 80–89.
[48] Q. Zhang, T. Wei, J. Lu, et al., J. Electroanal. Chem. 926 (2022) 116935.
[49] S. Li, Y. Gao, N. Li, et al., Energ. Environ. Sci. 14 (2021) 1897–1927.
[50] F. Yang, J. Dong, Z. Li, et al., ACS Nano 17 (2023) 4102–4133.
[51] L. Kong, M. Liu, H. Huang, et al., Adv. Energy Mater. 12 (2022) 2100172.
[52] G. Ou, Y. Xu, B. Wen, et al., Nat. Commun. 9 (2018) 1302.
[53] Y. La, Y. Cui, D. Lin, Nat. Nanotechnol. 12 (2017) 194–206.
[54] Q. Li, B. Quan, W. Li, et al., Nano Energy 45 (2018) 463–470.
[55] W. Cao, J. Lu, K. Zhou, Nano Energy 95 (2022) 106983.
[56] R. Zhang, X. Shen, Y. Zhang, J. Energy Chem. 71 (2022) 29–35.
[57] M. Srout, M. Carboni, J.A. Gonzalez, et al., Small 19 (2022) e2206252.
[58] X. Yu, Z. Li, X. Wu, et al., Joule 7 (2023) 1145–1175.
[59] H. Zhang, J. Chen, G. Zeng, et al., Nano Lett. 23 (2023) 3565–3572.
[60] H. Zhang, J. Chen, Y. Hong, et al., Nano Lett. 22 (2022) 9972–9981.